Dalton Transactions

ROYAL SOCIETY OF CHEMISTRY

PAPER

View Article Online
View Journal | View Issue

Cite this: *Dalton Trans.*, 2022, **51**, 16119

AIE-active Ir(III) complexes functionalised with a cationic Schiff base ligand: synthesis, photophysical properties and applications in photodynamic therapy†

Shengnan Liu, ‡[a] Jiahong Han,‡[a] Weijin Wang,[a] Yulei Chang, *[b] Runlin Wang,[a] Ziwei Wang,[a] Guangzhe Li,*[c] Dongxia Zhu *[a] and Martin R. Bryce *[d]

Photodynamic therapy (PDT) is a promising cancer treatment method. Traditional small-molecule photosensitizers (PSs) suffer from low intersystem crossing (ISC) ability and aggregation-caused quenching (ACQ), which adversely affects the luminous efficiency and singlet oxygen ($^1O_2$) yield of PSs in the aggregated state. Ir(III) complexes are promising PSs with long excited-state lifetime, good photophysical and photochemical properties and large Stokes shifts. Aggregation-induced emission (AIE) characteristics could reduce the nonradiative recombination and improve the ISC ability of excited states through the restriction of the intramolecular motions in aggregated states. Accordingly, two AIE-active Ir(III) complexes **Ir-1-N$^+$** and **Ir-2-N$^+$** were successfully designed and obtained based on Schiff base ligands. Experimental results showed that **Ir-1-N$^+$** and **Ir-2-N$^+$** have good photophysical properties and the corresponding nanoparticles (NPs) have good water solubility and $^1O_2$ generation ability. Notably, **Ir-2-N$^+$** NPs can be efficiently taken up by mouse breast cancer cells (4T1 cells) with good biocompatibility, low dark toxicity and excellent phototoxicity. This work demonstrates a versatile strategy for exploiting efficient transition metal PSs with a cationic ligand in PDT.

Received 9th September 2022,
Accepted 30th September 2022

DOI: 10.1039/d2dt02960j

rsc.li/dalton

Introduction

Photodynamic therapy (PDT) is a new method of cancer treatment that has attracted much attention in recent years. Its main process is that photosensitizers (PSs) accumulated in the tumor produce cytotoxic reactive oxygen species (ROS) to kill cancer cells or microorganisms while irradiated by light of specific wavelengths.[1–3] Nevertheless, most of the current PSs, such as boron dipyrromethene (BODIPY) and porphyrin derivatives, need long irradiation times and large amount of PSs to achieve the high generation of ROS owing to their low singlet-to-triplet intersystem crossing (ISC) ability, which limits their PDT efficacy.[4–6] The ISC rate depends upon the spin–orbital coupling (SOC) interaction between the lowest triplet and one or more singlet excited states. Because the SOC constant generally increases with atomic number, large SOC interactions are found in molecules comprising heavy atoms and SOC is therefore quite large for Ir (3909 cm^{-1}).[7,8] Compared with organic small-molecule PSs, Ir(III) complexes have the benefit of larger Stokes shifts that can reduce the interference between excited and emitted states.[9–11] At the same time, Ir(III) complexes also have high photochemical stability, which effectively avoids the shortcoming of photobleaching that organic small molecule PSs suffer from. In addition, long excited-state lifetime, high luminescence efficiency and tuneable emission color mean that Ir(III) complexes attract extensive attention as PSs.[12–14] However, Ir(III) complexes also have several disadvantages that severely limit their efficacy in PDT such as poor water solubility, limited biocompatibility and aggregation-caused quenching (ACQ) of emission.

Many available PSs have large π-electron systems and planar molecular structures which result in ACQ.[15] Meanwhile, the

[a]*Key Laboratory of Nanobiosensing and Nanobioanalysis at Universities of Jilin Province, Department of Chemistry, Northeast Normal University, 5268 Renmin Street, Changchun, Jilin Province 130024, P. R. China. E-mail: zhudx047@nenu.edu.cn*
[b]*State Key Laboratory of Luminescence and Applications, Changchun Institute of Optics, Fine Mechanics and Physics, Chinese Academy of Sciences, Changchun, Jilin Province 130033, China. E-mail: yuleichang@ciomp.ac.cn*
[c]*Jilin Provincial Science and Technology Innovation Center of Health Food of Chinese Medicine, Changchun University of Chinese Medicine, Changchun, Jilin Province 130117, P. R. China. E-mail: 1993008106@qq.com*
[d]*Department of Chemistry, Durham University, Durham, DH1 3LE, UK. E-mail: m.r.bryce@durham.ac.uk*

†Electronic supplementary information (ESI) available: Supporting figures and tables. See DOI: https://doi.org/10.1039/d2dt02960j

‡The authors contributed equally to the preparation of this work.

molecules suffer from other problems such as complicated synthetic and purification processes, poor solubility, low yield, weak absorption and low quantum efficiency.[16] However, the phenomenon of aggregation-induced emission (AIE) based on restricted intramolecular motion was promoted by Ben Zhong Tang and his team in 2001[17] and has subsequently been extensively discussed and developed as an important feature in many types of luminescent molecules.[18–23] PSs with AIE characteristics circumvent the above problems of traditional PSs in the aggregated state and have the following advantages: (i) improved ISC ability of excited states, (ii) high photoluminescence quantum efficiency (PLQY), (iii) high ROS generation ability.[24–26] Up till now there are only very few AIE Ir(III) complexes reported as PSs, indicating that it is still a challenge to realize their potential in cell and animal imaging, bacterial therapy and anti-tumor applications.[27,28]

Schiff bases have the advantages of easy modification, simple and efficient synthesis method. Many Schiff bases with different properties and variable structures can be derived by changing the substituent groups.[29–31] The presence of the imine bond makes Schiff bases one of the most widely used ligands in coordination chemistry with good coordination ability with most metal elements.[32–34] These ligands and their complexes have a wide range of applications in the biological field, including antioxidant, anti-cancer, antibacterial and others.[35–37] Therefore, Schiff bases have been used as versatile building blocks to construct AIE molecules.[38–40]

In this work, two AIE-active complexes **Ir-1-N$^+$** and **Ir-2-N$^+$** were obtained by a straightforward synthetic method with easy purification in high yields by using a chalcone Schiff base as auxiliary ligand.[41] The cationic quaternary amine functionality in **Ir-1-N$^+$** and **Ir-2-N$^+$** was designed to enhance hydrophilicity, cellular uptake and internalization of the PSs, by analogy with other ionic transition metal complexes.[42–44] The introduction of a quinolone–triphenylamine derivative as the cyclometalating ligand aims to increase the molar absorption and the singlet oxygen ($^1O_2$) generation ability of **Ir-2-N$^+$**. The corresponding nanoparticles (NPs) **Ir-1-N$^+$** NPs and **Ir-2-N$^+$** NPs were prepared by self-assembly process with poloxamer (F127) as surfactant. Both **Ir-1-N$^+$** NPs and **Ir-2-N$^+$** NPs have good water solubility and $^1O_2$ generation capacity. Spectroscopic studies and *in vitro* experiments show that **Ir-2-N$^+$** NPs have good biocompatibility, high photo-cytotoxicity that can be applied to PDT effects in the future.

Experimental section

Materials and instruments

Materials for organic synthesis, poloxamer (F127) and indocyanine green (ICG) were purchased from Energy Chemical Company. RPMI Medium 1640 was purchased from Solarbio Life Science company. Fetal bovine serum (FBS) was purchased from Sigma-Aldrich. 3-(4,5-Dimethylthiazol-2-yl)-2,5-diphenyltetrazolium bromide (MTT) was obtained from Aladdin. 2′,7′-Dichlorofluorescence diacetate (DCFH-DA) and the cell viability (live dead cell staining) assay kit were purchased from Shanghai Beyotime Biotechnology Co. Ltd.

^{1}H NMR spectra were recorded at 25 °C on a Varian 600 MHz spectrometer. The high resolution mass spectra (HRMS) were obtained on a high-performance liquid chromatography-high-resolution time of flight mass spectrometer (MicroTOF II). UV-vis absorption spectra were recorded on a Shimadzu UV-3100 spectrophotometer. The photoluminescence spectra, excited state lifetimes (τ) and photoluminescence quantum yields (Φ_{PL}) were recorded on an Edinburgh FLS920 spectrofluorimeter under air at room temperature. Transmission electron microscopy (TEM) images were taken by a TECNAI F20 microscope. Diameter and diameter distribution of the nanoparticles were determined by a Malvern Zetasizer Nano instrument for dynamic light scattering (DLS). Confocal laser scanning microscopy (CLSM) images were taken using a ZeissLSM 700 (Zurich, Switzerland).

The structures of complexes **Ir-1-N$^+$** and **Ir-2-N$^+$** are shown in Scheme 1 and the synthesis and characterization are reported in the ESI† with ^{13}C{^{1}H}NMR spectra (Fig. S1–S8†) and mass spectra (Fig. S9–S12†).

Preparation of nanoparticles (NPs)

The water-soluble NPs were prepared by the solvent exchange method. Firstly, metal iridium complex **Ir-1-N$^+$**/**Ir-2-N$^+$** (1 mg) and the surfactant F127 were dissolved in THF (1 mL). The mixture was dropped into deionized water (10 mL). The solution was stirred at a constant speed to evaporate the THF; after the THF was completely volatilized, the solution was put into a dialysis bag to remove the residual THF. Further filtration was performed with a 0.22 μm filter head to obtain uniformly dispersed nanoparticles. The concentration of nanoparticles was then calculated using a standard curve. The hydrodynamic sizes and morphologies of the NPs were analyzed by dynamic light scattering (DLS) and transmission electron microscopy (TEM).

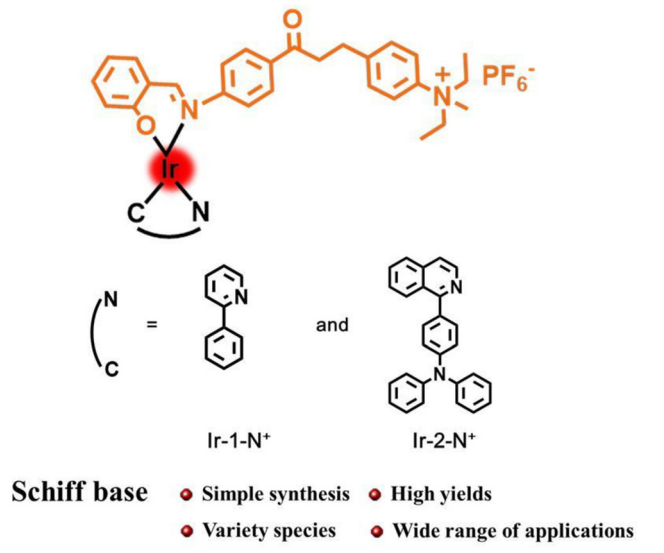

Scheme 1 Structures of **Ir-1-N$^+$** and **Ir-2-N$^+$**.

Test method for singlet oxygen generation in solution

The effect of PDT can be evaluated by the $^1O_2$ generation capacity in the solution. In these experiments, ICG was used as an indicator to evaluate the $^1O_2$ generation capacity of **Ir-1-N$^+$** and **Ir-2-N$^+$** and the corresponding NPs in solution. **Ir-1-N$^+$** and **Ir-2-N$^+$** solutions (15 μg mL^{-1} in CH_3CN–water (v/v) = 4/1) and their corresponding NPs solutions (15 μg mL^{-1} in water) were mixed with ICG solution (5 μg mL^{-1}) as working solutions. The working solution (3 mL) was transferred to a cuvette, and then was illuminated with a 425 nm LED at 20 mW cm^{-2} for 300 s.

Cell culture method

Mouse breast cancer cells (4T1 cells) were selected as the cell model for these experiments. The culture medium was prepared by RPMI Medium 1640 containing 10% (v : v) FBS. The cell culture flask was placed in an incubator at 37 °C and 5% CO_2. To ensure adequate nutrition for the cells, the culture medium was changed every two days.

Cytotoxicity test method

The cytotoxicity of PSs was detected by MTT. 4T1 cells were seeded in 96-well plates at a density of 10 000 cells per well. The cells were cultured in an incubator at 37 °C and 5% CO_2 for 24 h. After aspirating the old culture medium, RPMI Medium 1640 (100 μL) containing different concentration gradient PSs (0–10 μg mL^{-1}) was added to each well. The original culture medium was replaced by fresh RPMI Medium 1640 (100 μL) after 6 h. The light group was irradiated with 425 nm LED at 20 mW cm^{-2} for 30 min, while the dark group was not illuminated. After irradiation, the cells were placed in an incubator for 24 h. MTT (10 μL) with the concentration of 5 mg mL^{-1} was added to each well. The cells were placed in an incubator for 4 h. After 4 h, DMSO (200 μL) was added to each well to replace the original medium. The absorbance value of the sample at 490 nm was detected by a microplate reader.

Live/dead staining test methods

4T1 cells were seeded in confocal dishes at the density of 50 000 cells per well and incubated for 24 h. After the culture medium was aspirated, RPMI Medium 1640 containing PSs (10 μg mL^{-1}) was added to the confocal dish. After culturing for 6 h, the culture medium containing PSs was removed and fresh RPMI Medium 1640 was added. The light group was irradiated with 425 nm LED at 20 mW cm^{-2} for 30 min, and the dark group was treated the same without illumination. After illumination, the confocal dish was placed in the incubator and incubation was continued overnight. PBS was used to wash the confocal dishes. Detection buffer containing Calcein-AM and PI was added to the confocal dishes. This was followed by incubation in the dark in the incubator for 30 min. The fluorescence image was observed under an inverted fluorescence microscope to judge the cell survival state.

Evaluation of intracellular singlet oxygen production capacity

The ability of PSs to generate intracellular $^1O_2$ was assessed by DCFH-DA. 4T1 cells were seeded in confocal dishes at a density of 50 000 cells per well and incubated for 24 h. The next procedure was to aspirate the original medium and add RPMI Medium 1640 (1 mL) containing PSs (10 μg mL^{-1}) to the confocal dish. After continuing to culture in the incubator for 6 h, the supernatant was removed and RPMI 1640 was added. The light group was irradiated with 425 nm LED at 20 mW cm^{-2} for 15 min, and the dark group was treated in the same way without illumination. After light exposure, the original medium was aspirated, washed twice with PBS, and then DCFH-DA (1 μL) was dissolved in blank RPMI Medium 1640 without FBS and added to the confocal culture dish. After treatment in the dark for 20 min, the medium containing DCFH-DA was aspirated, washed twice with PBS (1 mL), and PBS (1 mL) was added, followed by CLSM to observe the green fluorescence intensity in the cells.

Test method for endocytic behavior

4T1 cells were seeded in confocal culture dishes at a density of 50 000 cells per well. A cell suspension (1 mL) containing RPMI Medium 1640 was added to each well. The cells were then placed in an incubator at 37 °C and 5% CO_2 overnight. The original medium was replaced by RPMI Medium 1640 containing PSs (10 μg mL^{-1}). The incubation time was 0.5 h, 2 h and 6 h, respectively. After incubation, the supernatant was withdrawn and the confocal culture dish was washed twice with PBS, and the uptake of PSs by cells was observed by CLSM.

Results and discussion

Photophysical properties

The photophysical properties of **Ir-1-N$^+$** and **Ir-2-N$^+$** were analyzed by UV-Vis absorption and emission spectroscopy. As shown in Fig. 1, both **Ir-1-N$^+$** and **Ir-2-N$^+$** have two absorption bands. The relatively strong absorption band in the range of 250–350 nm originates from the π–π* transition of the ligand center. The relatively weak absorption band in the 350–500 nm range can be attributed to spin-allowed metal-to-ligand charge-transfer transition (^{1}MLCT), spin-allowed ligand-to-ligand charge-transfer transition (^{1}LLCT), spin-forbidden metal-to-

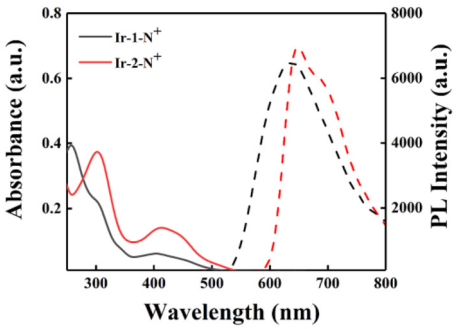

Fig. 1 The UV–vis absorption spectra in CH_3CN (solid line) and the PL spectra in the mixed solvent (CH_3CN–H_2O = 1 : 9) of **Ir-1-N$^+$** and **Ir-2-N$^+$** (10^{-5} M) (dashed line).

ligand charge-transfer transition (^{3}MLCT) and spin-forbidden ligand-to-ligand charge transfer transition (^{3}LLCT).[10] From Fig. 1, the absorbance of **Ir-2-N$^+$** at 425 nm is significantly enhanced due to the introduction of the extended π-conjugated cyclometalated ligand (quinoline triphenylamine) in **Ir-2-N$^+$**.[45] Both complexes exhibit red emission at excitation wavelength 425 nm. The maximum emission peak of **Ir-1-N$^+$** is at 640 nm and **Ir-2-N$^+$** is at 660 nm, with the red-shifted emission of **Ir-2-N$^+$** ascribed to the π-extended ligand which is consistent with the changing trends of the UV-Vis absorption spectra of the two complexes. Compared with **Ir-1-N$^+$**, **Ir-2-N$^+$** shows a larger Stokes shift (245 nm). This is important because PSs with a large Stokes shift can improve the signal-to-noise ratio of imaging by reducing the interference from the background.[46] The photoluminescence quantum yields (PLQYs) and excited-state lifetimes of **Ir-1-N$^+$** and **Ir-2-N$^+$** were determined, and their corresponding photophysical data are summarized in Table S1.† The Ir(III) complexes exhibit high PLQYs and relatively long excited-state lifetimes. The PLQYs of **Ir-1-N$^+$** and **Ir-2-N$^+$** are 17% and 19%, respectively, and the excited-state lifetimes are 542.2 ns and 551.3 ns, respectively. Their excellent photophysical properties, especially the enhanced absorption band and large Stokes shift and long excited-state lifetime, endow the complexes with high potential as PSs.

Research on AIE phenomenon

The AIE performance of **Ir-1-N$^+$** and **Ir-2-N$^+$** was analysed in mixed solutions of CH_3CN and water, while the water content was varied in the range of 0–99%. As shown in Fig. 2, **Ir-1-N$^+$** and **Ir-2-N$^+$** show weak emission in pure CH_3CN, but emit bright red phosphorescence when the water content gradually increases to 80%, which is a typical AIE characteristic.[47] The AIE properties of **Ir-1-N$^+$** and **Ir-2-N$^+$** were further explored by transmission electron microscopy (TEM) and UV-Vis absorption spectroscopy. The morphology and particle size are shown in Fig. S14.† Only a very few small aggregates were observed in pure CH_3CN. When the water content is 99%, the agglomerates increase significantly and become larger. From the UV-Vis absorption spectra (Fig. S15†) the tail of the absorption spectrum is enhanced with the gradual increase of the water content, indicating the Mie scattering effect.[48] **Ir-1-N$^+$** and **Ir-2-N$^+$** possess excellent AIE characteristics according to the above results, originating from the effective restriction of non-radiative transitions, and these properties are beneficial for the ISC process and the generation of ROS.

Characterization of nanoparticles

Two water-soluble nanoparticles, **Ir-1-N$^+$** NPs and **Ir-2-N$^+$** NPs, were prepared by a solvent exchange method. As shown in Fig. S16,† the hydrated particle size of the NPs was measured using DLS. The data showed that the average particle sizes of **Ir-1-N$^+$** NPs and **Ir-2-N$^+$** NPs were 92 nm and 63 nm, respectively. According to the TEM images (Fig. 3), the NPs are spherical and the particle size is <100 nm. These properties make the NPs easily endocytosed by cells. Within a week, **Ir-1-N$^+$** NPs and **Ir-2-N$^+$** NPs exhibited negligible change in size and polydispersity indices (PDIs), indicating their good stability. The high stability of NPs facilitates better circulation in the blood. Therefore, **Ir-1-N$^+$** NPs and **Ir-2-N$^+$** NPs with good water solubility, suitable size and high stability are promising candidates for use in living cells and animal experiments.[49]

Evaluation of singlet oxygen generation capability in solution

The ability to generate $^1O_2$ is an important parameter to assess the effect of PDT. The $^1O_2$ generation capacity of **Ir-1-N$^+$**, **Ir-2-N$^+$** and their corresponding NPs was evaluated by monitoring the change in the absorbance of ICG at 790 nm. The data are shown in Fig. 4 and S17–S20,† for (1) the unirradiated group containing ICG and PSs; (2) the irradiated group containing only PSs; and (3) the irradiated group containing only ICG. The absorbance of ICG has no change within 300 s, indicating that **Ir-1-N$^+$** and **Ir-2-N$^+$** and their corresponding NPs have good photostability. Under irradiation conditions, the absorbance of ICG in the presence of **Ir-1-N$^+$** and **Ir-2-N$^+$** decreased. This reveals that $^1O_2$ is generated in irradiation conditions rather than in dark conditions. Compared with **Ir-1-N$^+$**, **Ir-2-N$^+$** shows higher $^1O_2$ generation ability, which could be because the absorbance of **Ir-2-N$^+$** at 425 nm is higher than that of **Ir-1-N$^+$**. After **Ir-1-N$^+$** and **Ir-2-N$^+$** were fabricated into NPs, their $^1O_2$ generation capacity was significantly higher than those of the corresponding "free" complexes. The data suggests that the ability to generate $^1O_2$ is increased in the aggregated state (Fig. 4). The $^1O_2$ generation capacities of **Ir-1-N$^+$** and **Ir-2-N$^+$**

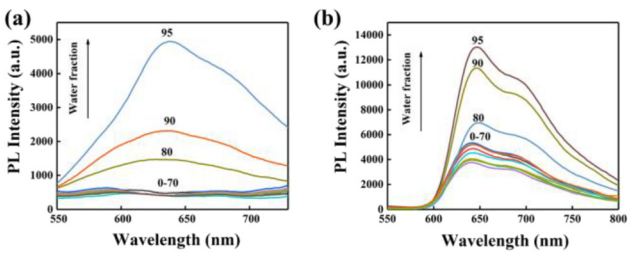

Fig. 2 PL spectra of **Ir-1-N$^+$** (a) and **Ir-2-N$^+$** (b) in CH_3CN–H_2O mixtures (complex concentration = 1.0 × 10^{-5} M) with different water fractions (0–95% v/v) at room temperature.

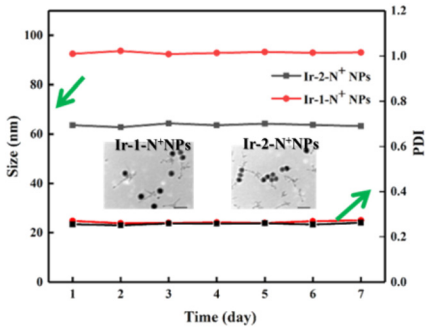

Fig. 3 DLS data of **Ir-1-N$^+$** NPs and **Ir-2-N$^+$** NPs during 7 days. Inset: TEM images of **Ir-1-N$^+$** NPs and **Ir-2-N$^+$** NPs.

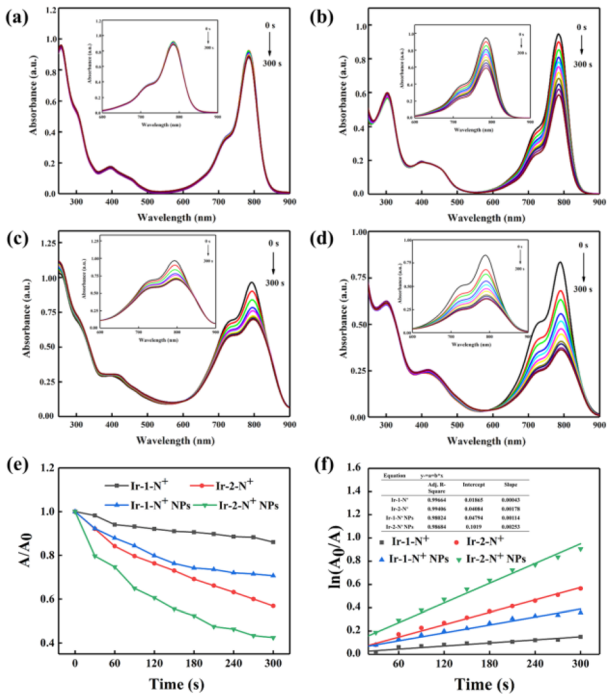

Fig. 4 The UV–vis absorption spectra of ICG (5 μg mL^{-1}) with **Ir-1-N$^+$** (a), **Ir-2-N$^+$** (b) **Ir-1-N$^+$** NPs (c) and **Ir-2-N$^+$** NPs (d). (e) The decay rates of ICG in the presence of **Ir-1-N** and **Ir-2-N** and their NPs upon exposure to light illumination (425 nm, 20 mW cm^{-2}). (f) Time-dependent $^1O_2$ generation kinetics. A_0 = initial absorbance maximum of ICG. A = real-time absorbance maximum of ICG with various light exposure times. An enlarged inset table is shown as Table S2 in ESI.†

and their corresponding NPs conform to first-order kinetics, with the slope **Ir-2-N$^+$** NPs > **Ir-2-N$^+$** > **Ir-1-N$^+$** NPs > **Ir-1-N$^+$**. The larger the slope, the faster the degradation rate of ICG, indicating the greater ability to generate $^1O_2$. Obviously, **Ir-2-N$^+$** NPs exhibited improved singlet oxygen generation ability and they have a high potential as PSs for clinical applications in the future. The above experiments establish that charged Ir(III) complexes with AIE properties based on a rational molecular design strategy demonstrate improved $^1O_2$ generation ability for such kind of PSs.

Cytotoxicity studies

The cytotoxicity of **Ir-2-N$^+$** NPs in 4T1 cells was analyzed by using the 3-(4,5-dimethylthiazol-2-yl)-2,5-diphenyltetrazolium bromide (MTT) assay,[50] which is a quantitative colorimetric method. MTT is converted into purple formazan crystals by metabolizing the mitochondrial dehydrogenase of living cells, then dimethyl sulfoxide can dissolve the generated formazan. As shown in Fig. 5a, after the 4T1 cells were incubated overnight, they were treated with **Ir-2-N$^+$** NPs and had a viability of more than 90%, showing good biocompatibility and low dark toxicity. When irradiated by a 425 nm LED at 20 mW cm^{-2}, the cell viability decreased gradually with the increasing concentration of **Ir-2-N$^+$** NPs, showing a concentration-dependent cellular phototoxicity. When the concentration of **Ir-2-N$^+$** NPs reached 10 μg mL^{-1},

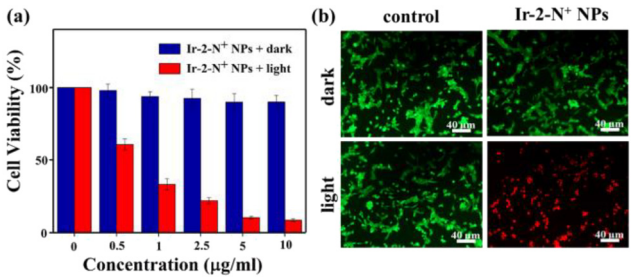

Fig. 5 (a) Relative viability of 4T1 cells after 24 h co-incubation with **Ir-2-N$^+$** NPs under darkness and under irradiation (425 nm, 20 mW cm^{-2}). (b) Confocal fluorescence images of 4T1 cells co-stained with Calcein-AM (live cells, green fluorescence) and propidium iodide (dead cells, red fluorescence) after treatment with **Ir-2-N$^+$** NPs (10 μg mL^{-1}).

the cell viability was only 10% under irradiation. The MTT experiments therefore showed that **Ir-2-N$^+$** NPs exhibited good phototoxicity and low dark toxicity in cell experiments.

Live/dead cell staining experimental study

We used the Calcein-AM and propidium iodide (PI) double fluorescence staining method to detect the PDT effect of **Ir-2-N$^+$** NPs in 4T1 cells.[51] Calcein-AM is a cell-permeable dye that is widely used to detect viability in most eukaryotic cells. PI cannot pass through the cell membrane of living cells and only can enter damaged cells, where it binds to nucleic acids and emits red fluorescence. Calcein-AM and PI were used simultaneously to detect live/dead cells. As shown in Fig. 5b, a strong green fluorescence signal and a very weak red fluorescence signal were observed in the dark for the blank control group and **Ir-2-N$^+$** NPs, indicating that **Ir-2-N$^+$** NPs have lower dark toxicity and good biocompatibility. However, strong red fluorescence signals and negligible green fluorescence signals were observed in 4T1 cells pre-treated with **Ir-2-N$^+$** NPs under irradiation, indicating that almost all 4T1 cells were killed. Both live/dead cell staining experiments and MTT experiments showed that the conversion of AIE iridium complexes into the corresponding NPs can effectively improve the biocompatibility and PDT effect of the complexes.

Evaluation of intracellular singlet oxygen production capacity

2,7-Dichlorodihydrofluorescein diacetate (DCFH-DA) does not emit light. However, when it enters cells, it is hydrolyzed by intracellular esterase and converted to 2,7-dichlorodihydrofluorescein (DCFH) which can react with $^1O_2$ to generate the green fluorescent molecule 2,7-dichlorofluorescein (DCF).[52] The greater the amount of singlet oxygen, the stronger the fluorescent signal generated. The intensity of the green fluorescence can be used to judge the ability of the PSs to generate $^1O_2$ in the cell. Therefore, we used DCFH-DA to detect the formation of $^1O_2$ in 4T1 cells after illumination. As shown in Fig. 6, no green fluorescence was produced in the blank control and **Ir-2-N$^+$** NPs under dark conditions. After 15 min of illumination, the cells in the **Ir-2-N$^+$** NPs group showed obvious green fluorescence, while the blank control group still

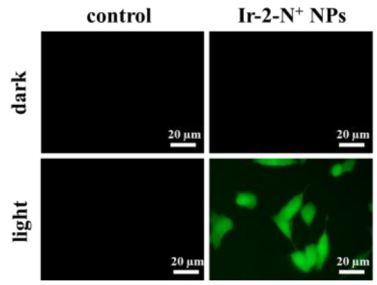

Fig. 6 Confocal fluorescence images for the detection of $^1O_2$ generation in 4T1 cells treated with **Ir-2-N$^+$** NPs under darkness and under irradiation (425 nm, 20 mW cm^{-2}).

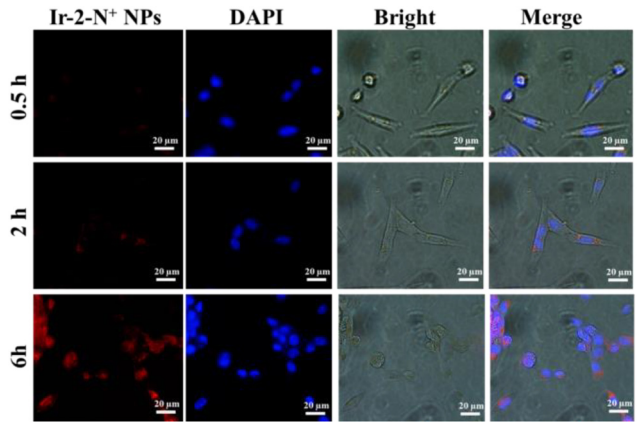

Fig. 7 Cellular uptake of **Ir-2-N$^+$** NPs (10 μg mL^{-1}) detected by CLSM at different periods of time.

had no fluorescence. The result shows that **Ir-2-N$^+$** NPs cannot produce $^1O_2$ under dark conditions, but they can effectively generate $^1O_2$ in the cells after illumination. The good $^1O_2$ generation ability of **Ir-2-N$^+$** NPs indicates that **Ir-2-N$^+$** NPs have good application potential as PSs in PDT.

Endocytosis studies

We further characterized the cellular uptake behavior of **Ir-2-N$^+$** NPs using CLSM (Fig. 7). Since the particle size of **Ir-2-N$^+$** NPs is <100 nm, they can readily enter cells. The phosphorescence signal generated in the cells gradually increased with the extension of the culture time, indicating that the cellular uptake was time-dependent. At 6 h, 4T1 cells incubated with **Ir-2-N$^+$** NPs had a strong red phosphorescence signal due to the large Stokes shift of **Ir-2-N$^+$**, which gives a good imaging effect. Endocytosis experiments demonstrated that **Ir-2-N$^+$** NPs could be efficiently taken up by 4T1 cells and had good biocompatibility. The efficient uptake of PSs by cells is a premise for good PDT.

Conclusions

In summary, two Ir(III) complexes with a pendant quaternary ammonium cation and their NPs with AIE properties were designed and synthesized utilizing a Schiff base ligand. The synthetic routes to **Ir-1-N$^+$** and **Ir-2-N$^+$** are simple and high yielding. The complexes were successfully used as PSs in the study of PDT. The introduction of quinoline triphenylamine as the cyclometalated ligands enhances the absorption of **Ir-2-N$^+$**; the emission is red-shifted and the ability to generate $^1O_2$ is significantly improved relative to the phenylpyridine analogue **Ir-1-N$^+$**. Owing to the AIE features of the Ir(III) complexes, the **Ir-1-N$^+$** NPs and **Ir-2-N$^+$** NPs, which are in the aggregated state of **Ir-1-N$^+$** and **Ir-2-N$^+$**, exhibit higher $^1O_2$ generation capacity than their corresponding small molecules. Among them, **Ir-2-N$^+$** NPs which exhibit bright red emission, efficient $^1O_2$ generation ability, good water solubility, excellent phototoxicity, and negligible dark toxicity are shown to be good PSs *in vitro* for PDT. This work provides a meaningful design strategy for obtaining AIE self-assembled cationic transition metal complex NPs with red light emission as efficient PSs for PDT.

Conflicts of interest

There are no conflicts to declare.

Acknowledgements

This work was funded by NSFC (Grants No. 52073045, 51773195, 62075217), the Key Scientific and Technological Project of Jilin Province (20190701010GH), Jilin Provincial Department of Science and Technology (Grants 20210101148JC), the Development and Reform Commission of Jilin Province (2020C035-5), and Changchun Science and Technology Bureau (CC202110378310002101). M. R. B. thanks EPSRC (UK) grant EP/L02621X/1 for funding. D. Zhu is grateful for the support from the Key Laboratory of Nanobiosensing and Nanobioanalysis at the Universities of Jilin Province. The authors acknowledge the support from the Jilin Provincial Department of Education.

References

1 H. Zhao, L. Li, F. Li, C. Liu, M. Huang, J. Li, F. Gao, X. Ruan and D. Yang, *Adv. Mater.*, 2022, **34**, e2109920.
2 D. Wang, H. Wang, L. Ji, M. Xu, B. Bai, X. Wan, D. Hou, Z. Y. Qiao, H. Wang and J. Zhang, *ACS Nano*, 2021, **15**, 8694–8705.
3 M. Huo, P. Liu, L. Zhang, C. Wei, L. Wang, Y. Chen and J. Shi, *Adv. Funct. Mater.*, 2021, **31**, 2010196.
4 Z. Yu, H. Wang, Z. Chen, X. Dong, W. Zhao, Y. Shi and Q. Zhu, *J. Med. Chem.*, 2022, **65**, 3616–3631.
5 V. Ramu, P. Kundu, P. Kondaiah and A. R. Chakravarty, *Inorg. Chem.*, 2021, **60**, 6410–6420.
6 Y. X. Li, Y. Liu, H. Wang, Z. T. Li and D. W. Zhang, *ACS Appl. Bio Mater.*, 2022, **5**, 881–888.
7 *Iridium(III) in Optoelectronic and Photonics Applications*, ed. E. Zysman-Colman, John Wiley and Sons, Chichester, 2017.

8 M. Montalti, A. Credi, L. Prodi and M. T. Gandolfi, *Handbook of Photochemistry*, Taylor and Francis, Boca Raton, FL, 3rd edn, 2006.
9 G. Lu, Z. G. Wu, R. Wu, X. Cao, L. Zhou, Y. X. Zheng and C. Yang, *Adv. Funct. Mater.*, 2021, **31**, 2102898.
10 Y. Luo, Z. Liu, G. Yang, T. Wang, Z. Bin, J. Lan, D. Wu and J. You, *Angew. Chem., Int. Ed.*, 2021, **60**, 18852–18859.
11 H. Shin, Y. H. Ha, H. G. Kim, R. Kim, S. K. Kwon, Y. H. Kim and J. J. Kim, *Adv. Mater.*, 2019, **31**, e1808102.
12 C. Jin, G. Li, X. Wu, J. Liu, W. Wu, Y. Chen, T. Sasaki, H. Chao and Y. Zhang, *Angew. Chem., Int. Ed.*, 2021, **60**, 7597–7601.
13 J. Shen, J. Karges, K. Xiong, Y. Chen, L. Ji and H. Chao, *Biomaterials*, 2021, **275**, 120979.
14 J. Zhao, K. Yan, G. Xu, X. Liu, Q. Zhao, C. Xu and S. Gou, *Adv. Funct. Mater.*, 2020, **31**, 2008325.
15 K. Zheng, G. B. Bodedla, Y. Hou, J. Zhang, R. Liang, J. Zhao, D. Lee Phillips and X. Zhu, *J. Mater. Chem. A*, 2022, **10**, 4440–4445.
16 B. M. Luby, C. D. Walsh and G. Zheng, *Angew. Chem., Int. Ed.*, 2019, **58**, 2558–2569.
17 J. Luo, Z. Xie, J. W. Lam, L. Cheng, H. Chen, C. Qiu, H. S. Kwok, X. Zhan, Y. Liu, D. Zhu and B. Z. Tang, *Chem. Commun.*, 2001, 1740–1741.
18 J. Mei, N. L. C. Leung, R. T. K. Kwok, J. W. Y. Lam and B. Z. Tang, *Chem. Rev.*, 2015, **115**, 11718–11940.
19 L. Meng, X. Ma, S. Jiang, S. Zhang, Z. Wu, B. Xu, Z. Lei, L. Liu and W. Tian, *CCS Chem.*, 2021, **3**, 2084–2094.
20 S. Du, G. Pan, S. Dai, B. Xu and W. Tian, *Aggregate*, 2021, **2**, e96.
21 F. Würthner, *Angew. Chem., Int. Ed.*, 2020, **59**, 14192–14196.
22 G. R. Suman, M. Pandey and A. S. J. Chakravarthy, *Mater. Chem. Front.*, 2021, **5**, 1541–1584.
23 Y. Luo, S. Zhang, H. Wang, Q. Luo, Z. Xie, B. Xu and W. Tian, *CCS Chem.*, 2022, **4**, 456–463.
24 D. Mao and B. Liu, *Matter*, 2021, **4**, 350–376.
25 D. Li, Y. Li, Q. Wu, P. Xiao, L. Wang, D. Wang and B. Z. Tang, *Small*, 2021, **17**, e2102044.
26 Q. Wan, R. Zhang, Z. Zhuang, Y. Li, Y. Huang, Z. Wang, W. Zhang, J. Hou and B. Z. Tang, *Adv. Funct. Mater.*, 2020, **30**, 2002057.
27 L. Zhang, Y. Li, W. Che, D. Zhu, G. Li, Z. Xie, N. Song, S. Liu, B. Z. Tang, X. Liu, Z. Su and M. R. Bryce, *Adv. Sci.*, 2019, **6**, 1802050.
28 J. Zhao, S. Sun, X. Li, W. Zhang and S. Gou, *ACS Appl. Bio Mater.*, 2020, **3**, 252–262.
29 H. Chen, C. Huang, Y. Deng, Q. Sun, Q. L. Zhang, B. X. Zhu and X. L. Ni, *ACS Nano*, 2019, **13**, 2840–2848.
30 J. Zhang, L. Xu and W.-Y. Wong, *Coord. Chem. Rev.*, 2018, **355**, 180–198.
31 T. A. J. Grell, A. P. Young, C. L. Drennan and V. Bandarian, *J. Am. Chem. Soc.*, 2018, **140**, 6842–6852.
32 M. A. Malik, S. A. Lone, M. Y. Wani, M. I. A. Talukdar, O. A. Dar, A. Ahmad and A. A. Hashmi, *Bioorg. Chem.*, 2020, **98**, 103771.
33 R. E. Malekshah, F. Shakeri, A. Khaleghian and M. Salehi, *Int. J. Biol. Macromol.*, 2020, **152**, 846–861.
34 X. Liu and J.-R. Hamon, *Coord. Chem. Rev.*, 2019, **389**, 94–118.
35 D. Ling, H. Li, W. Xi, Z. Wang, A. Bednarkiewicz, S. T. Dibaba, L. Shi and L. Sun, *J. Mater. Chem. B*, 2020, **8**, 1316–1325.
36 Y. Liang, Z. Li, Y. Huang, R. Yu and B. Guo, *ACS Nano*, 2021, **15**, 7078–7093.
37 Y. Liang, M. Li, Y. Yang, L. Qiao, H. Xu and B. Guo, *ACS Nano*, 2022, **16**, 3194–3207.
38 S. Guieu, F. Cardona, J. Rocha and A. M. S. Silva, *Chem. – Eur. J.*, 2018, **24**, 17262–17267.
39 D. Li, X. Liang, F. Zhang, J. Li, Z. Zhang, S. Wang, Z. Li, Y. Xing and K. Guo, *J. Mater. Chem. C*, 2022, **10**, 11016–11026.
40 S. Lin, H. Pan, L. Li, R. Liao, S. Yu, Q. Zhao, H. Sun and W. Huang, *J. Mater. Chem. C*, 2019, **7**, 789–7899.
41 S. Liu, J. Han, Y. Chang, W. Wang, R. Wang, Z. Wang, G. Li, D. Zhu and M. R. Bryce, *Chem. Commun.*, 2022, **58**, 10056–10059.
42 R. E. Daniels, L. K. McKenzie, J. R. Shewring, J. A. Weinstein, V. N. Kozhevnikov and H. E. Bryant, *RSC Adv.*, 2018, **8**, 9670–9676.
43 Y. Ma, S. Zhang, H. Wei, Y. Dong, L. Shen, S. Liu, Q. Zhao, L. Liu and W.-Y. Wong, *Dalton Trans.*, 2018, **47**, 5582–5588.
44 B. Hou, W. Zhang, C. Li, X. Sun, X. Feng and J. Liu, *Appl. Organomet. Chem.*, 2022, **36**, e6598.
45 Z. Liu, S. W. Zhang, M. Zhang, C. Wu, W. Li, Y. Wu, C. Yang, F. Kang, H. Meng and G. Wei, *Front. Chem.*, 2021, **9**, 758357.
46 W. Wang, K. J. Wu, K. Vellaisamy, C. H. Leung and D. L. Ma, *Angew. Chem., Int. Ed.*, 2020, **59**, 17897–17902.
47 Y. Wang, T. Yang, X. Liu, G. Li, W. Che, D. Zhu and Z. Su, *J. Mater. Chem. C*, 2018, **6**, 12217–12223.
48 B. Xu, W. Li, J. He, S. Wu, Q. Zhu, Z. Yang, Y. C. Wu, Y. Zhang, C. Jin, P. Y. Lu, Z. Chi, S. Liu, J. Xu and M. R. Bryce, *Chem. Sci.*, 2016, **7**, 5307–5312.
49 Z. Zhang, W. Xu, M. Kang, H. Wen, H. Guo, P. Zhang, L. Xi, K. Li, L. Wang, D. Wang and B. Z. Tang, *Adv. Mater.*, 2020, **32**, e2003210.
50 H. Lu, X. Jiang, Y. Chen, K. Peng, Y. Huang, H. Zhao, Q. Chen, F. Lv, L. Liu, S. Wang and Y. Ma, *Nanoscale*, 2020, **12**, 14061–14067.
51 N. K. Pandey, W. Xiong, L. Wang, W. Chen, B. Bui, J. Yang, E. Amador, M. Chen, C. Xing, A. A. Athavale, Y. Hao, W. Feizi and L. Lumata, *Bioact. Mater.*, 2022, **7**, 112–125.
52 J. Deng, H. Li, M. Yang and F. Wu, *Photochem. Photobiol. Sci.*, 2020, **19**, 905–912.